

## Research



**Cite this article:** Llorens M-G, Griera A, Steinbach F, Bons PD, Gomez-Rivas E, Jansen D, Roessiger J, Lebensohn RA, Weikusat I. 2017 Dynamic recrystallization during deformation of polycrystalline ice: insights from numerical simulations. *Phil. Trans. R. Soc. A* **375**: 20150346.

<http://dx.doi.org/10.1098/rsta.2015.0346>

Accepted: 10 November 2016

One contribution of 11 to a theme issue 'Microdynamics of ice'.

### Subject Areas:

glaciology

### Keywords:

ice rheology, dynamic recrystallization, ice microstructure, non-basal activity, strain hardening

### Author for correspondence:

Maria-Gema Llorens

e-mail: [maria-gema.llorens-verde@uni-tuebingen.de](mailto:maria-gema.llorens-verde@uni-tuebingen.de)

[uni-tuebingen.de](http://uni-tuebingen.de)

# Dynamic recrystallization during deformation of polycrystalline ice: insights from numerical simulations

Maria-Gema Llorens<sup>1,2</sup>, Albert Griera<sup>3</sup>, Florian Steinbach<sup>1,2</sup>, Paul D. Bons<sup>1</sup>, Enrique Gomez-Rivas<sup>4</sup>, Daniela Jansen<sup>2</sup>, Jens Roessiger<sup>1</sup>, Ricardo A. Lebensohn<sup>5</sup> and Ilka Weikusat<sup>1,2</sup>

<sup>1</sup>Department of Geosciences, Eberhard Karls University Tübingen, Tübingen, Germany

<sup>2</sup>Alfred Wegener Institute for Polar and Marine Research, Bremerhaven, Germany

<sup>3</sup>Departament de Geologia, Universitat Autònoma de Barcelona, Barcelona, Spain

<sup>4</sup>School of Geosciences, University of Aberdeen, Aberdeen, UK

<sup>5</sup>Material Science and Technology Division, Los Alamos National Laboratory, Los Alamos, NM, USA

 MGL, 0000-0002-6148-2600; EGR, 0000-0002-1317-6289; IW, 0000-0002-3023-6036

The flow of glaciers and polar ice sheets is controlled by the highly anisotropic rheology of ice crystals that have hexagonal symmetry (ice Ih). To improve our knowledge of ice sheet dynamics, it is necessary to understand how dynamic recrystallization (DRX) controls ice microstructures and rheology at different boundary conditions that range from pure shear flattening at the top to simple shear near the base of the sheets. We present a series of two-dimensional numerical simulations that couple ice deformation with DRX of various intensities, paying special attention to the effect of boundary conditions. The simulations show how similar orientations of *c*-axis maxima with respect to the finite deformation direction develop regardless of the amount of DRX and applied boundary conditions. In pure shear this direction is parallel to the maximum compressional stress, while it rotates towards the shear direction in simple shear. This

leads to strain hardening and increased activity of non-basal slip systems in pure shear and to strain softening in simple shear. Therefore, it is expected that ice is effectively weaker in the lower parts of the ice sheets than in the upper parts. Strain-rate localization occurs in all simulations, especially in simple shear cases. Recrystallization suppresses localization, which necessitates the activation of hard, non-basal slip systems.

This article is part of the themed issue 'Microdynamics of ice'.

## 1. Introduction

Ice is one of the most common minerals found at the Earth's surface. Most of it is concentrated in polar ice sheets, formed originally from precipitation of snow. Owing to its ductile behaviour, ice flows towards the ice sheet margins driven by gravity. While this behaviour is commonly described by continuum-mechanical approaches, its underlying processes are of crystallographic nature, where deformation takes place by dislocation creep [1]. At terrestrial conditions, single ice crystals have a hexagonal symmetry (ice Ih) and deform plastically by preferential glide of dislocations along the basal planes of the hexagonal lattice, where the slip of dislocations is almost isotropic. The stress required to activate dislocation glide along non-basal slip systems is about 60 times higher than that for the basal one [2], when subjected to similar strain rates.

Natural ice usually occurs in the form of polycrystalline aggregates, which develop a *c*-axis preferred orientation during deformation. This process is facilitated by recrystallization of the ice grains, as polar ice is always at high homologous temperatures (i.e. near to the melting point). The microstructural evolution of the mineral aggregate during deformation leads to progressively anisotropic macroscopic behaviour (e.g. [3]). The development of a fabric or a lattice preferred orientation (LPO) due to deformation influences the response of ice layers to imposed stresses [4], deforming an order of magnitude faster than an equivalent isotropic polycrystal in simple shear deformation. We define LPO here as the statistically preferred orientation of the crystalline lattices of a population of grains [5]. Activation of recrystallization processes during plastic deformation (dynamic recrystallization, DRX) can enhance ice flow, modifying the microstructure (defined as the collection of all microscopic deformation-related structures and the orientation stereology of polycrystals [5]) and LPO [6,7], or activating non-basal slip systems [8]. It is, therefore, critical to understand how DRX influences ice microstructures at different boundary conditions, because microstructural changes are related to climatic transitions in the palaeoclimate record stored in ice sheets [9].

Natural ice deformation fabrics and microstructures can be studied with different techniques. Firstly, the analysis of ice microstructures measured from ice core samples provides an insight into the nature of strongly deformed natural ice. There are abundant data from the upper 100 m of ice cores, where firn transitions into ice. However, only a limited number of datasets from deep ice cores exist. Very few campaigns have been able to acquire deep ice samples, because they are expensive and logistically demanding (see [5] for an overview). Furthermore, coring sites are preferably located in very special strain environments, mainly in zones of ice divides and domes. This is because deformation in these zones mostly takes place under vertical compression (e.g. pure shear or axial compression) as the ice is buried under annual snow layers. These locations are specifically chosen to get relatively undisturbed layers to extract the clearest possible palaeoclimate signals. Therefore, the deformation regimes that are subjected to high shear strain rates, which are found at the flanks or outlets of the ice sheets, are usually not prioritized for deep drilling campaigns, as this regime gives rise to folding of ice layers [9–12]. However, it is critical that we understand how ice behaves in all the parts of ice sheets and not only in ice divides and domes. Only few ice coring projects have focused to date on recovering samples with the aim of studying ice flow properties [13,14]. The EGRIP campaign will soon recover ice samples from the onset region of an ice stream (EGRIP website: <http://eastgrip.org/>).

Experiments are another widely used technique to learn about ice rheology during deformation and recrystallization. Samples of natural or artificial ice are deformed under controlled strain or stress boundary conditions and at a certain temperature in order to understand the processes that govern deformation and the resulting microstructures. These methods have significantly contributed to our understanding of ice rheology [15–17]. However, experiments are limited to certain geometries and usually do not achieve high finite strains. Another disadvantage here is that experimental samples are subjected to much higher strain rates ( $\dot{\epsilon}$ ) than natural ice, especially in the case of slowly flowing polar ice sheets ( $\dot{\epsilon} \approx 10^{-10}$ – $10^{-13} \text{ s}^{-1}$  [13,18]). As the viscosity of ice depends on the applied stress and this relation is highly nonlinear, other techniques should be used in order to complement our understanding of ice rheology [19].

Numerical simulations provide a tool to fill in the gaps left by the study of natural and experimental ice deformation, because simulations are not limited by scale, stress or strain rate. Moreover, numerical models allow the systematic investigation of different aspects of DRX on ice flow, based on the underlying physical processes [20]. In this way, it is possible to link processes on the dislocation scale to the behaviour of ice at the scale of the polycrystal. Additionally, by evaluating the relation between stress and strain rate from the bulk behaviour at the mesoscopic (centimetre to metre) scale, we can also establish links with the macroscopic scale. Furthermore, modelling allows the comparison of ice rheology under different boundary conditions, such as pure- and simple-shear deformation. Thus, microstructural modelling can be a valuable addition to the analysis of ice microstructures in natural ice samples and laboratory experiments.

Despite the importance of DRX on the behaviour of natural ice, theoretical and computational studies have been restricted mostly to the simulation of (i) ice deformation at the scale of single crystals [21] or (ii) deformation of polycrystalline materials using finite-element methods, whereby isotropic rheological properties are used to model crystal plasticity [22,23].

The full-field formulation based on fast Fourier transforms (FFT) [24] has proved to be a successful alternative modelling tool to simulate plastic deformation of polycrystals [25,26], especially when coupled with algorithms for DRX processes [8,27]. Viscoplastic full-field numerical modelling (in short VPFFT modelling) of the evolution of a polycrystalline aggregate under controlled strain boundary conditions can be applied to investigate the relative importance of deformation mechanisms and recrystallization processes on the development of ice fabrics and flow (e.g. [20]). Here we use the VPFFT formulation inside the modelling platform ELLE [28,29], which has been widely used to model processes in rocks and has recently been adapted to experiments on polycrystals with the characteristics of natural ice. The aim of this paper is to present the state of the art of the VPFFT/ELLE modelling of ice, paying particular attention to the effect of vorticity boundary conditions (i.e. pure versus simple shear) and DRX.

## 2. Numerical procedure

### (a) ELLE numerical platform

The software platform ELLE [28,29] was used to perform the simulations presented in this contribution. The ELLE software is open source and can be downloaded from the online repository (<http://www.elle.ws>). ELLE processes reproduce the evolution of microstructures during deformation and metamorphism, such as grain growth [30–32], DRX [8,33,34], folding [12,27,35,36] and rotation of rigid objects in anisotropic materials [37,38].

In this contribution, we compare the microstructural evolution of ice Ih during viscoplastic deformation and recrystallization. The numerical approach is based on the coupling of (i) a full-field viscoplastic code that uses a FFT approach (VPFFT [25,39]) to calculate the viscoplastic deformation of the polycrystalline aggregate and (ii) the microstructural modelling platform ELLE for the simulation of DRX.

Two main layers define the data structure of the models: (i) a contiguous set of polygons (figure 1*a,b*) that are used to define grains and that are themselves defined by straight boundary

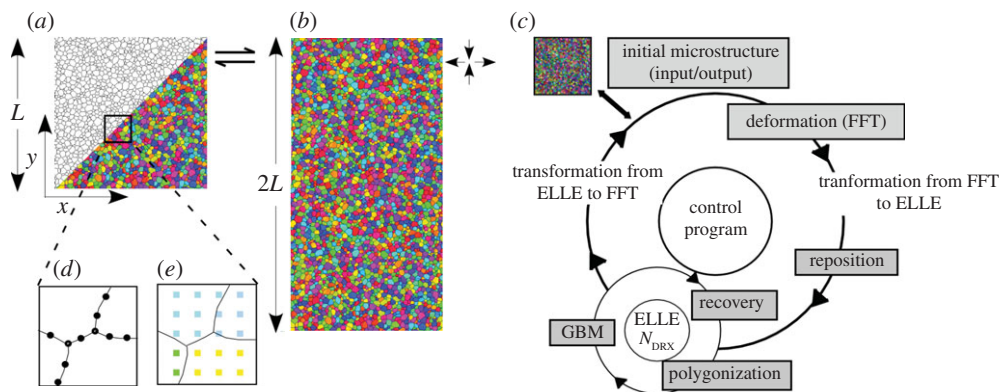


**Figure 1.** Initial microstructures showing the ELLE data layers and program flow. The initial microstructure in simple shear simulations is a square model defined by a side of one-unit length ( $L$ ) (a), while in pure shear simulations the initial size of the model is duplicated vertically ( $2L$ ) (b) to allow better visualization of the deformed microstructure. (d) Detail of boundary nodes (*bnodes*) defining grains and (e) detail of *unodes* or Fourier points. (c) The microstructure goes through a loop of processes every time step: deformation by small increments of dextral simple shear or vertical shortening in pure shear simulations, reposition that brings the model back into the unit cell and a subloop of DRX processes (grain boundary migration, recovery and polygonization). (Online version in colour.)

segments joined at boundary nodes (*bnodes*; figure 1d) and (ii) a high-resolution grid of unconnected nodes (*unodes*) that store physical properties within grains, such as the local lattice orientation, defined by three Euler angles, and the dislocation density (figure 1e). These *unodes* also serve as Fourier points to simulate crystallites for the viscoplastic deformation calculations [25]. The data structure of the VPFPT and ELLE codes is fully wrapping: grains touching one side of the model continue on the other side. Two different sets of initial microstructures are used to investigate three series of simulations (table 1): a single-phase ice polycrystalline aggregate with a cell size of  $L \times L$  to be deformed in simple shear (figure 1a) and an  $L \times 2L$  cell to be deformed in pure shear vertical shortening (figure 1b). A grid density of  $256 \times 256$  *unodes* was used to define a unit cell, resulting in a total of 65 536 discrete *unodes*. Grains initially have a random lattice orientation (figure 1a–c), representing a bulk isotropic material.

In our approach, each small time increment ( $\Delta t$ ) is represented by a sequential loop of processes. For all the simulations presented, an experimental run (figure 1c) consists of iterative applications of an incremental 0.02 natural strain, defined as  $\ln(L_f/L_i)$ , equivalent to 2% of shortening of vertical coaxial compression or an incremental shear strain of  $\Delta\gamma = 0.04$  in simple shear simulations. The deformation step is followed by a subloop of DRX, where grain boundary migration (GBM), recovery and polygonization processes are activated. Since the mobility parameter of recrystallization processes and time step are the same for all simulations, we model deformation at different strain rates by varying the ratio between the viscoplastic deformation step and the DRX step, activating the DRX subloop  $N_{\text{DRX}} = 0, 1, 10, 20$  or 25 times per deformation time step (see values in table 1). When DRX is not active it is not possible to calculate the strain rate, because there is no time step defined in the model. When DRX is active,  $N_{\text{DRX}}$  is inversely proportional to the strain rate. Using the parameters defined further below, the  $N_{\text{DRX}}$  correspond to strain rates ranging from  $3.17 \times 10^{-11}$  down to  $1.27 \times 10^{-12} \text{ s}^{-1}$ .

The first series of simulations (labelled by PSH  $N_{\text{DRX}}$ ) models DRX, including GBM and recovery, of ice under pure-shear vertical shortening up to a natural strain of 1.2. This series includes a simulation (PSH 20\_N) that incorporates polygonization. The second series (SSH  $N_{\text{DRX}}$ ) simulates DRX of ice, including GBM and recovery, under dextral simple shear conditions up to a natural strain of 1.2. This series includes simulations (SSH 1\_N and SSH 10\_N) that incorporate polygonization. The simulation set-up is listed in table 1. Lattice orientation data, as

**Table 1.** Set-up of the two series of numerical simulations.

name	DRX/VPFFT ratio ( $N_{\text{DRX}}$ )	ELLE processes	strain rate ( $\text{s}^{-1}$ )
first series (PSH $N_{\text{DRX}}$ )			
experiment PSH 0	0	GBM + recovery	—
experiment PSH 1	1	GBM + recovery	$3.17 \times 10^{-11}$
experiment PSH 10	10	GBM + recovery	$3.17 \times 10^{-12}$
experiment PSH 20	20	GBM + recovery	$1.00 \times 10^{-10}$
experiment PSH 20_N	20	GBM + recovery + polygonization	$1.00 \times 10^{-10}$
experiment PSH 25	25	GBM + recovery	$1.27 \times 10^{-12}$
second series (SSH $N_{\text{DRX}}$ )			
experiment SSH 0	0	GBM + recovery	—
experiment SSH 1	1	GBM + recovery	$3.17 \times 10^{-11}$
experiment SSH 1_N	1	GBM + recovery + polygonization	$3.17 \times 10^{-11}$
experiment SSH 10	10	GBM + recovery	$3.17 \times 10^{-12}$
experiment SSH 10_N	10	GBM + recovery + polygonization	$3.17 \times 10^{-12}$
experiment SSH 25	25	GBM + recovery	$1.27 \times 10^{-12}$

well as misorientation and activity of slip systems fields, were plotted using the texture analysis software MTEX [40].

## (b) Fast Fourier transform: viscoplastic deformation by dislocation glide

VPFFT provides a strain rate and stress field that minimizes the average local work rate under compatibility and equilibrium constraints [25,39]. VPFFT is a full-field crystal plasticity formulation that explicitly resolves velocity and stress fields, assuming that deformation is accommodated by dislocation glide only. The constitutive relation between the strain rate  $\dot{\epsilon}_{ij}(\mathbf{x})$  and the deviatoric stress  $\sigma'(\mathbf{x})$  at a point  $\mathbf{x}$  of the Fourier grid is given by

$$\dot{\epsilon}_{ij}(\mathbf{x}) = \sum_{s=1}^{N_s} m_{ij}^s(\mathbf{x}) \dot{\gamma}^s(\mathbf{x}) = \dot{\gamma}_0 \sum_{s=1}^{N_s} m_{ij}^s(\mathbf{x}) \left| \frac{m^s(\mathbf{x}) : \sigma'(\mathbf{x})}{\tau^s(\mathbf{x})} \right|^n \text{sgn}(m^s(\mathbf{x}) : \sigma'(\mathbf{x})), \quad (2.1)$$

where the sum runs over all ( $N_s$ ) slip systems  $s$  in the crystal,  $m^s$  is the symmetric Schmid tensor,  $\tau^s$  is the resistance to slip or critical resolved shear stress,  $\dot{\gamma}^s$  is the shear strain rate,  $\dot{\gamma}_0$  is a reference strain rate and  $n$  is the rate sensitivity or stress exponent in Glen's law [41]. To simulate the mechanical properties of a polycrystalline aggregate of ice Ih crystals, a mineral with hexagonal symmetry and deformation accommodated by glide of dislocations along basal and non-basal slip systems (i.e. prismatic and pyramidal) is assumed. The degree of anisotropy ( $A$ ) is defined by the ratio between the critical resolved shear stresses  $\tau^s$  between the non-basal and the basal slip systems.  $A$  is approximately 60 according to Duval *et al.* [2], but the basal slip system is assumed to be 20 times weaker than the pyramidal and prismatic ones ( $A=20$ ) in all the simulations presented here. This value of  $A$  is a compromise to avoid too long a calculation time, while still maintaining an acceptable accuracy of the result [8]. The rate sensitivity exponent is  $n=3$  for all the slip systems. The resulting micromechanical fields from VPFFT are used to estimate the geometrically necessary dislocation density and deformation-induced lattice rotation, required inputs to simulate intra-crystalline recovery and GBM.

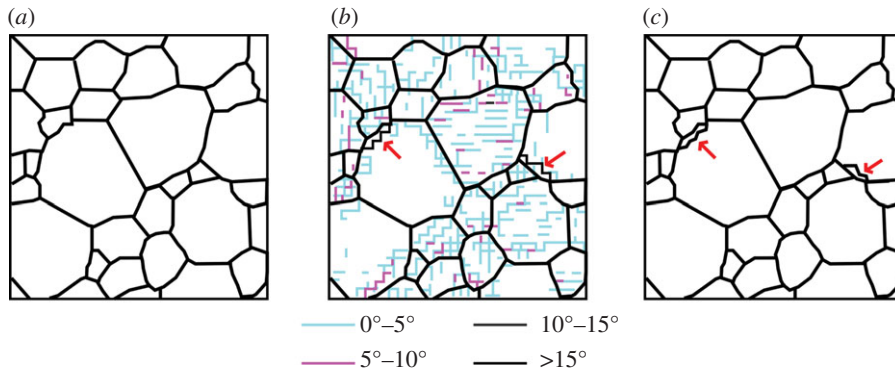


**Figure 2.** Example of the polygonization routine. (a) The initial microstructure has grains with homogeneous lattice orientations inside grains (no misorientation). (b) After one step of simple shear deformation LAGB (cyan, magenta and dark grey lines) and new HAGB (black lines) have developed. (c) The polygonization routine identifies the HAGB (more than  $15^\circ$ ) and updates the grain boundary network. Red arrows indicate newly nucleated grains. (Online version in colour.)

### (c) ELLE: recrystallization processes

After each deformation step, recrystallization is simulated by means of three processes: polygonization, GBM and recovery. The polygonization routine creates new high-angle grain boundaries (HAGB) when a cluster of *unodes* within a grain have a misorientation angle with respect to the parent grain that is higher than a critical pre-defined angle. GBM is driven by the reduction of grain boundary energy and stored strain energy, reproducing the motion or displacement of HAGB [42]. Recovery reduces the intra-granular stored energy in a deformed crystal, simulating annihilation of dislocations and their rearrangement into low-angle subgrain boundaries (LAGB) [43].

#### (i) Polygonization

The polygonization routine modifies the *bnodes* layer through splitting a pre-existing grain by inserting new boundary nodes. This process commences with a routine that identifies subgrains, i.e. clusters of *unodes* with misorientation values above a pre-defined threshold (HAGB more than  $15^\circ$ ; figure 2b). Once a critical subgrain is detected, the position of its boundary is obtained using a Voronoi tessellation of the cluster of *unodes* clipping the boundary to the pre-existing grain. A convex hull routine is used to define the smallest convex polygon enclosing the Voronoi points and clipped boundary nodes. The use of Voronoi decomposition allows us to prevent topological errors in the network of grains.

#### (ii) Grain boundary migration

GBM is modelled according to the front tracking approach explained in more detail in [8,33]. GBM is driven by a reduction of surface energy and stored strain energy. The driving stress ( $\Delta f$ ) is derived from the internal strain energy ( $\Delta H$ ) and the total grain boundary surface energy, which depends on the surface energy ( $J$ ) and the local radius of curvature ( $r$ ) of the grain boundary:

$$\Delta f = \Delta H - \frac{2J}{r}. \quad (2.2)$$

The velocity ( $v$ ) of the grain boundary is calculated from the driving stress ( $\Delta f$ ) and grain boundary mobility ( $M$ ) such that the work done equals the change in the local energy state:

$$v = M\Delta f n, \quad (2.3)$$

where  $\mathbf{n}$  is a unit vector in the direction of movement. The mobility is highly dependent on temperature ( $T$ ) and it is calculated from the intrinsic mobility ( $M_0 = 0.023 \text{ m}^2 \text{ kg}^{-1} \text{ s}^{-1}$  [44]), the grain boundary diffusion activation energy ( $Q = 40 \text{ kJ mol}^{-1}$  [45]) and the universal gas constant ( $R$ ):

$$M = M_0 \exp(-Q/RT). \quad (2.4)$$

The stored energy ( $\Delta H$ ) is calculated from the difference in dislocation density across a grain boundary ( $\Delta\rho$ ), the shear modulus ( $G$ , assumed to be isotropic) and the Burgers vector ( $\mathbf{b}$ ):

$$\Delta H = \Delta\rho G|\mathbf{b}|^2. \quad (2.5)$$

This routine picks single *bnodes* in a random order and uses four orthogonal small trial moves (parallel to the  $x$ - and  $y$ -axes, and of  $1/100$  of the average distance between *bnodes*) of that *bnode* to determine the direction ( $\mathbf{n}$ ) with the maximum driving stress ( $\Delta f$ ) [33]. The *bnode* is then moved over a small distance,  $v \cdot \Delta t$ , in the direction of  $\mathbf{n}$  according to equation (2.3). In areas swept by the moving boundary, the stored strain energy ( $\Delta H$ ) is reduced to zero.

### (iii) Recovery

The recovery module that simulates intra-granular reduction of the stored strain energy is applied after GBM. The recovery routine implemented in ELLE [43] simulates annihilation of dislocations and their rearrangement into LAGB. This process assumes that each *unode* represents a small crystallite or potential subgrain. The rotation rate of the lattice within the crystallite is proportional to the torque applied on the sides of the crystallite. This torque is calculated from the angular mismatch of the *unode* and its neighbours, which results in an effective interface energy [46]. The algorithm, described in detail in [8], is applied to an *unode* and its neighbours that belong to the same grain. The lattice orientation of the reference *unode* is rotated towards the value that results in the maximum reduction in interface energy calculated from trial rotations. This procedure is repeated for each *unode* in random order.

## 3. Results

### (a) Microstructure evolution

At the end of the simulations (natural strain of  $\varepsilon = 1.2$ ) differences in grain size and grain shape are observed. They reflect the different strain rates applied and the concomitant differences in the activity of DRX (table 2). The case of ice deformation without DRX is represented by experiments PSH 0 and SSH 0, for pure and simple shear boundary conditions, respectively. In both cases, viscoplastic deformation leads to the development of a grain shape preferred orientation (SPO) by the irregular elongation of grains oriented parallel to the stretching direction (figure 3*a,e*). This direction is the horizontal  $x$ -axis in pure shear models, while in simple shear models it rotates clockwise from  $45^\circ$  with respect to  $x$  at the beginning of the simulations towards the shear direction that is parallel to the  $x$ -axis. Deformation localization in the simple shear models produces strongly elongated grains in high-strain bands, which form at low angle with respect to the shear direction (figure 3*a*). In pure shear models conjugate sets of such high-strain bands are observed, but oriented symmetrically with respect to the vertical maximum shortening direction (figure 3*e*). In both cases, the high-strain bands are obliquely oriented with respect to the grain SPO. These bands are additionally characterized by high values of misorientations (i.e. intra-granular heterogeneities calculated as the angular difference in lattice orientation between an *unode* and its neighbours), progressively developing high local misorientations and recognizable subgrains, as can be seen in the misorientation field maps (figure 3*e*).

Different degrees of DRX were simulated in experiments PSH and SSH 1, 10 and 25, where the number refers to  $N_{\text{DRX}}$ , i.e. the number of recrystallization steps per VPFFT steps in the loop. The activation of GBM and recovery produces a general grain size coarsening, with grains becoming more equant with decreasing strain rate (table 2 and figure 3*b-d,f-h*). As a result, the grain

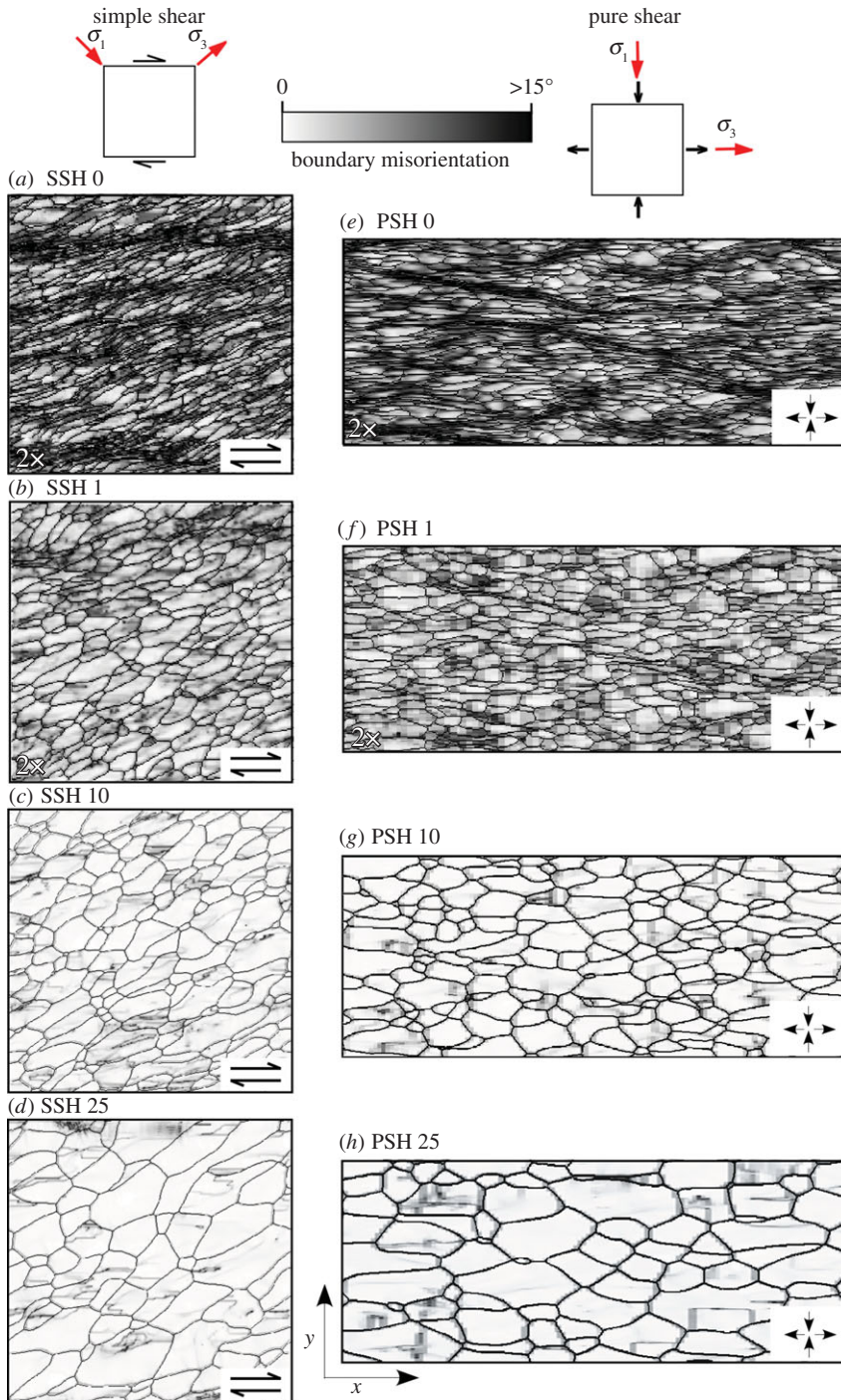


**Figure 3.** Comparison of the grain boundary network and local misorientation field at a natural strain of  $\varepsilon = 1.2$  for simulations deformed in simple shear (a–d) and pure shear (e–h), with (a,e) no recrystallization, (b,f) 1 step, (c,g) 10 steps and (d,h) 25 steps of recrystallization per deformation step, respectively, indicated by the  $N_{DRX}$  suffix (or ratio DRX/VPFFT). The initial microstructure is shown in figure 1a,b. In pure shear simulations (e–h), the original image length is double that of the images shown. For better visibility, figures for experiments 0 and 1, both in simple (SSH) and pure shear (PSH), have been enlarged two times, only showing the upper left quarter of each model. (Online version in colour.)

**Table 2.** Grain average values.

name	initial average grain area (mm <sup>2</sup> )	final number grains	final average grain area (mm <sup>2</sup> )	standard deviation (mm <sup>2</sup> )
first series (PSH)				
experiment PSH 0	6.12	3321	6	4
experiment PSH 1	6.12	1949	10	8
experiment PSH 10	6.12	365	55	42
experiment PSH 20	6.12	1160	6	5
experiment PSH 20_N	6.12	1631	12	12
experiment PSH 25	6.12	145	138	105
second series (SSH)				
experiment SSH 0	6.12	1636	6	4
experiment SSH 1	6.12	873	12	9
experiment SSH 1_N	6.12	1943	5	6
experiment SSH 10	6.12	156	64	55
experiment SSH 10_N	6.12	490	20	21
experiment SSH 25	6.12	61	163	122

SPO qualitatively weakens, but preferred elongation of grains parallel to the stretching direction is still recognizable in models that have up to  $N_{\text{DRX}} = 25$  steps per deformation increment (figure 3*b–d,f–h*). A reduction of the local misorientation by the arrangement of subgrain domains results in the development of low-angle boundaries and lower intra-granular heterogeneities than in models with  $N_{\text{DRX}} = 0$ . Subgrain size generally tends to increase with  $N_{\text{DRX}}$ . Contrary to what can be observed in models without recrystallization, bands with highly stretched grains do not develop in other simulations, except in models with  $N_{\text{DRX}} = 1$ . However, these bands are small compared with those in models that only include deformation. In the models  $N_{\text{DRX}} = 10$  and  $N_{\text{DRX}} = 25$ , these bands are not recognizable and grain size distributions are relatively uniform. In general, grain boundaries show straight to smooth geometries. Triple junctions are typically characterized by angles close to  $120^\circ$  with increasing  $N_{\text{DRX}}$ , but large deviations from this angle can still be qualitatively observed in the  $N_{\text{DRX}} = 25$  cases.

## (b) Lattice orientation evolution

Orientation maps and lattice orientation distributions at a natural strain of  $\varepsilon = 1.2$  are displayed in figure 4. Differences in lattice orientation are recognizable from colour differences according to inverse pole figures relative to the  $y$  direction of the sample. All simulations present a final similar LPO with respect to the finite deformation directions, regardless of the applied boundary conditions (vorticity) and amount of DRX. The initial randomly oriented grains (initial microstructure in figure 4) evolved towards an LPO approximately defined by  $c$ -axes (i.e.  $\{0001\}$  axes in figure 4*a–d*) parallel to the maximum shortening direction, or perpendicular to the foliation, while the  $a$ -axes (i.e.  $\{11\bar{2}0\}$  axes in figure 4) tend to be parallel to the stretching direction, or parallel to the foliation.

In the case of pure shear deformation, the  $c$ -axes maxima are oriented sub-parallel to the compression axis  $\sigma_1$  during all simulation time, displaying a broad single maximum for the PSH 0 case and becoming increasingly concentrated towards the  $y$ -axis with increasing DRX (see polar figures in figures 4*e–h* and 5*e–h*). In the case of simple shear deformation,  $c$ -axes are oriented

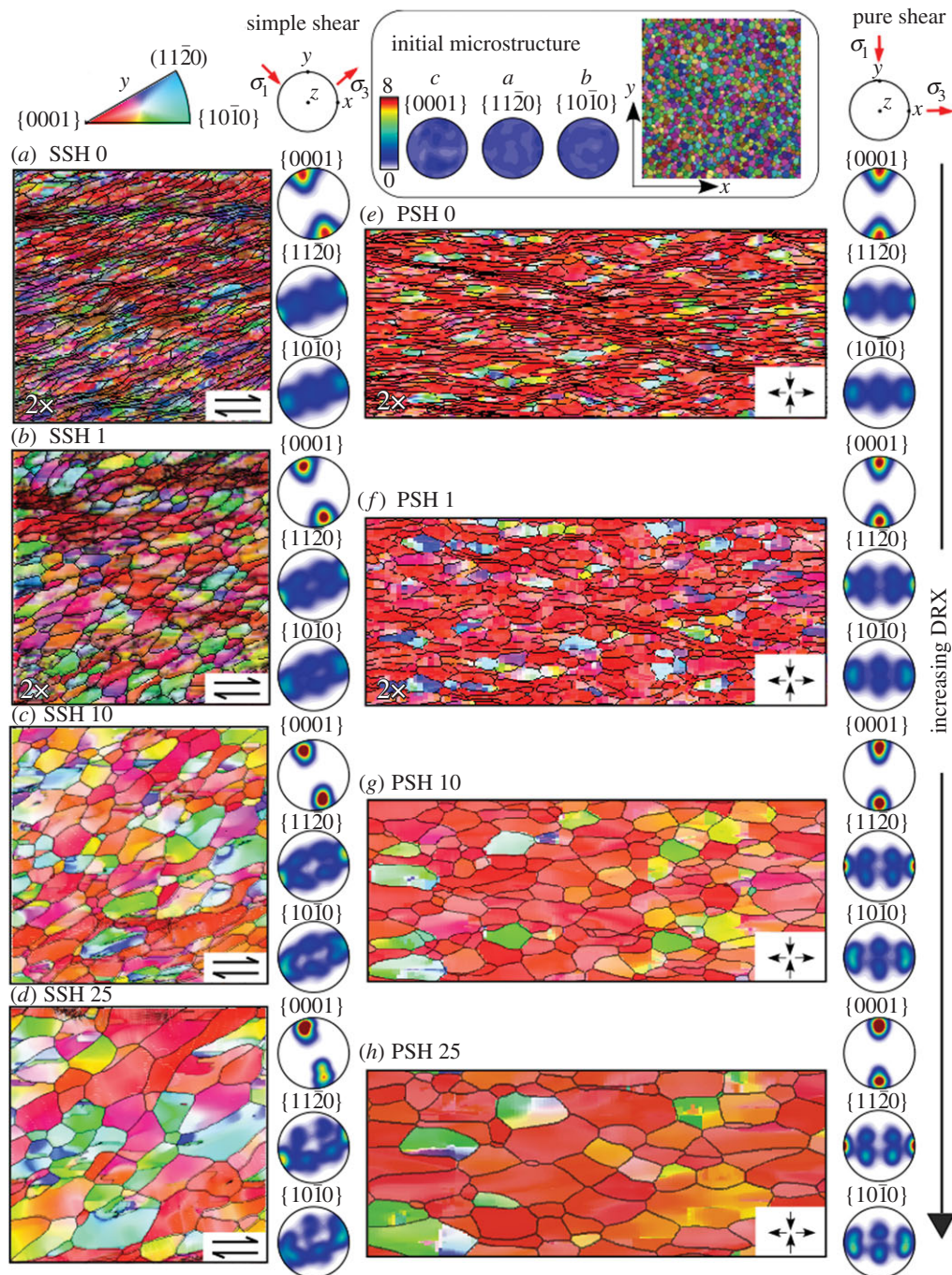


**Figure 4.** Lattice orientations relative to the  $y$ -direction (inverse poles) and pole figures of lattice orientation at natural strain of  $\varepsilon = 1.2$  for simulations of ice deformed in simple shear ( $a-d$ ) and pure shear ( $e-h$ ), with ( $a,e$ ) no recrystallization, ( $b,f$ ) 1 step, ( $c,g$ ) 10 steps and ( $d,h$ ) 25 steps of recrystallization per deformation step, respectively. Initial random distribution of lattice orientations is shown in the upper part of the figure. In pure shear simulations ( $e-h$ ), the original image length is double that of the images shown. In order to allow visualization of the microstructures, the figures of experiments 0 and 1, in both simple (SSH) and pure shear (PSH), have been enlarged two times, only showing the upper left quarter of each model. Lattice orientation figures include misorientation map and grain network. Pole figures show orientation of unodes. (Online version in colour.)

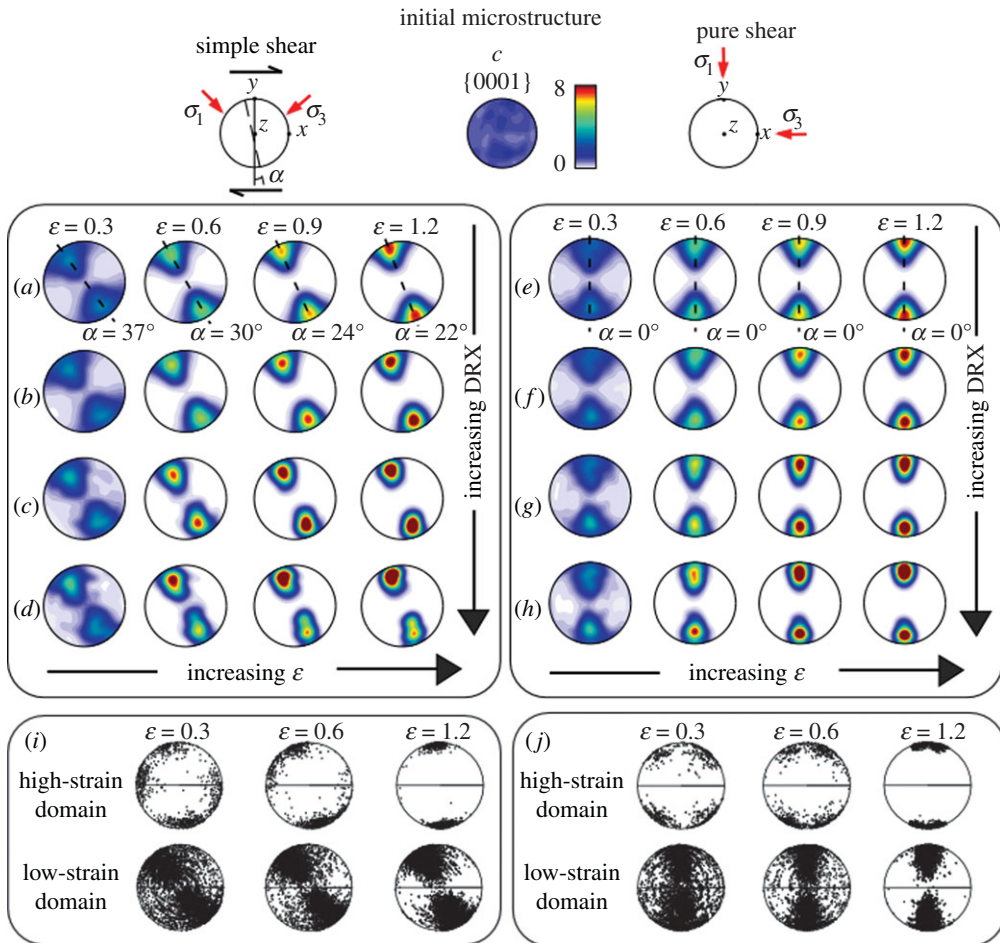


**Figure 5.** Pole figures of  $c$ -axes  $\{0001\}$  orientation at natural strains of  $\varepsilon = 0.3, 0.6, 0.9$  and the end of the simulations ( $\varepsilon = 1.2$ ) for simulations of ice deformed in simple shear ( $a-d,i$ ) and pure shear ( $e-h,j$ ) boundary conditions, with ( $a,e$ ) no recrystallization, ( $b,f$ ) 1 step, ( $c,g$ ) 10 steps and ( $d,h$ ) 25 steps of recrystallization per deformation step, respectively. The angle  $\alpha$  indicates the obliquity of the developed LPO with respect to the  $y$ -direction. The colour bar indicates the multiples of a uniform distribution. Pole figures of lattice orientation in high- and low-strain domains of simulations performed with no recrystallization in both pure and simple shear, respectively ( $i,j$ ). Pole figures show orientation of unodes. (Online version in colour.)

obliquely to the maximum compression axis and rotate in a synthetic sense (i.e. in the same way as the imposed shear sense) towards the normal to the shear plane (or sample  $y$ -axis) with progressive deformation. It has to be noted that this condition was not achieved at the end of the simulations (figure 5*a-d*). Apart from the orientation of the  $c$ -axis maximum with respect to  $\sigma_1$ , differences between pure and simple shear are remarkably subtle (figure 5). The fabric generally tends to be slightly weaker in pure shear models and displays a more marked girdle component than in simple shear cases.

When DRX is active, the LPO develops faster and  $c$ -axes tend to be slightly inclined with respect to the  $xy$ -plane in both pure and simple shear simulations (figure 5). The effect of DRX is more pronounced on the distributions of  $a$ - and  $b$ -axes, since they lie on a broad great circle in models with low DRX, and this trend is divided into a number of distinct maxima for cases with higher DRX. This result is coherent with the enhancement of the LPO single maximum.

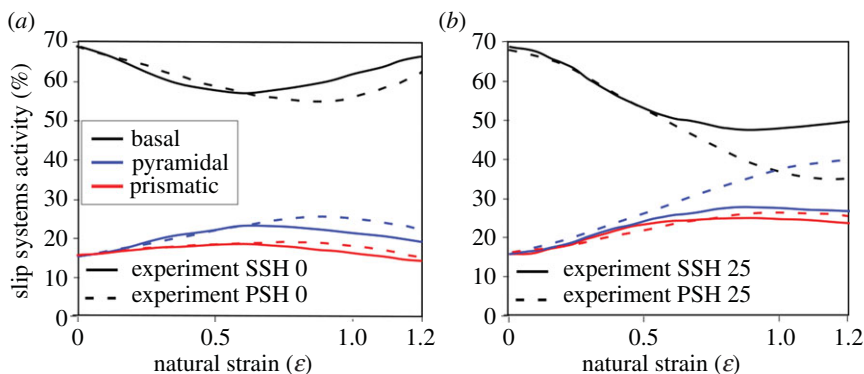


**Figure 6.** Evolution of the average relative slip system activity with progressive deformation for the simulations (a) without DRX ( $N_{DRX} = 0$ ) and (b) including DRX ( $N_{DRX} = 25$ ). (Online version in colour.)

### (c) Activity of the slip systems

In the absence of DRX, the activity of the basal slip systems is 60–70% higher than that of the non-basal slip systems in both pure and simple shear simulations (figure 6a). The basal slip system activity is concentrated in the high strain-rate bands, oriented at low angles to the horizontal shear plane in simple shear (figure 7a), or in conjugate bands distributed symmetrically around the vertical  $y$ -direction in pure shear simulations (figure 7c). When DRX is active the activity of the non-basal slip systems is increased in both pure and simple shear simulations, especially in pure shear (figure 6b). The slip system activity is not distributed in bands because they are destroyed by DRX. Larger grains, produced by GBM, contain subgrains with different amounts of basal (tilt and twist boundaries) and non-basal activity (figure 7b,d).

### (d) Rheology

All simulations show an increment of 30% or more in differential stress with increasing strain (i.e. strain hardening; figure 8a). Differential stress is defined as the difference between the maximum and minimum principal stresses. Significant deviations of the stress evolution between pure and simple shear only start developing after  $\epsilon \approx 0.5$ , where differential stress stabilizes in simple shear models (light lines in figure 8a) and continues increasing in the pure shear cases (dark lines in figure 8a). A similar hardening behaviour, but followed by weakening at higher strain, was observed in simple shear deformation of polycrystalline aggregates of olivine [47,48] and quartz [49], and also in numerical simulations of two-phase materials [50]. Differences between laboratory experiments and numerical simulations are discussed further in §4b.

### (e) Strain localization

The observable strain localization in conjugate high-strain bands of strongly elongated grains (figure 3a,e) is quantified using a slight modification of the localization factor defined by Sornette *et al.* [51] and Gomez-Rivas [52]:

$$f = 1 - \frac{1}{n_t} \frac{(\sum_{n_i}^{n_t} \dot{\epsilon}_{vm})^2}{\sum_{n_i}^{n_t} \dot{\epsilon}_{vm}^2}, \quad (3.1)$$

where  $n_t$  the total number of unodes and  $\dot{\epsilon}_{vm}$  is the von Mises strain rate for every unode  $n_i$ , defined as

$$\dot{\epsilon}_{vm} = \sqrt{\frac{2}{3}} \dot{\epsilon}_{ij} \dot{\epsilon}_{ij}. \quad (3.2)$$

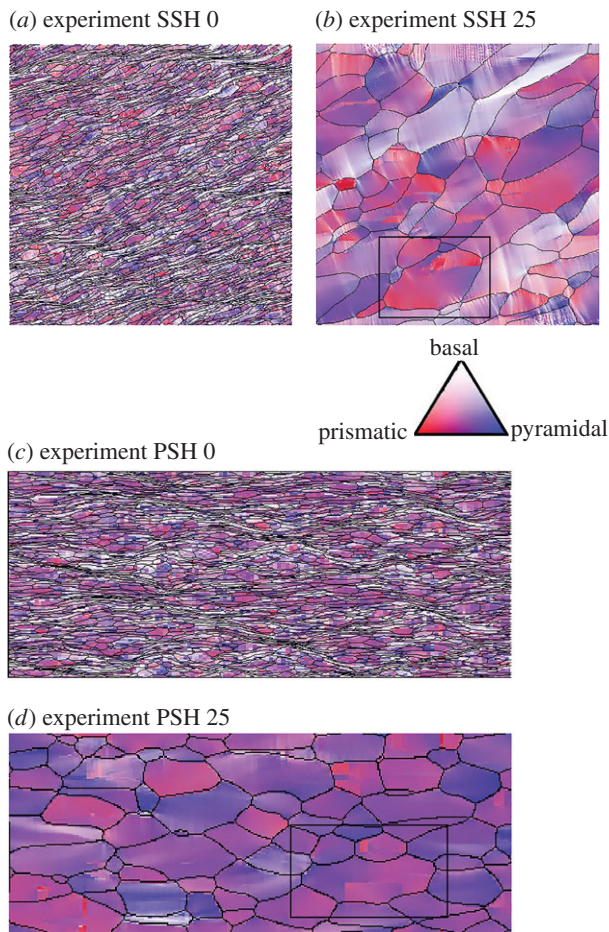


**Figure 7.** Maps of slip system activity for the last step of deformation (at  $\varepsilon = 1.2$ ) are shown for (a,b) simple shear and (c,d) pure shear simulations with  $N_{\text{DRX}} = 0$  and  $N_{\text{DRX}} = 25$ . In pure shear simulations (c,d) the original image length is double that of the images shown. Two examples of grains with subgrain boundaries developed by the activity of non-basal slip systems are marked in black squares in (b,d).

The strain localization factor ( $f$ ) can range from 0 to 1, where 0 represents homogeneous deformation and 1 maximum localization.

All simulations in simple shear show an initial trend towards more homogeneous deformation, followed by a reversal when localization strengthens again (figure 9a). DRX suppresses localization, with the reversal occurring at a higher strain in cases with higher  $N_{\text{DRX}}$ . Pure shear simulations are characterized by a steady state up to a natural strain of  $\varepsilon = 0.3$ , followed by either a reduction of localization at high  $N_{\text{DRX}}$  or an increase in localization when  $N_{\text{DRX}}$  is low (figure 9b). In general, DRX suppresses localization of deformation, but only after about a natural strain of  $\varepsilon = 0.3$ , when a distinct LPO starts to develop.

To show the strain-rate intensity, the von Mises strain rate is calculated as a function of the symmetric strain-rate tensor (equation (3.2)) and plotted in figure 10. In simple shear simulations high strain-rate synthetic bands oriented at low angles to the horizontal shear plane (also called synthetic shear bands) develop (figure 10a). In pure shear simulations, high strain-rate conjugate bands form at angles of  $66^\circ$ – $71^\circ$  with respect to the vertical  $y$ -direction (figure 10c). In both simple and pure shear models, the number and intensity of shear bands are reduced by DRX (experiment 25 in figure 10b,d).

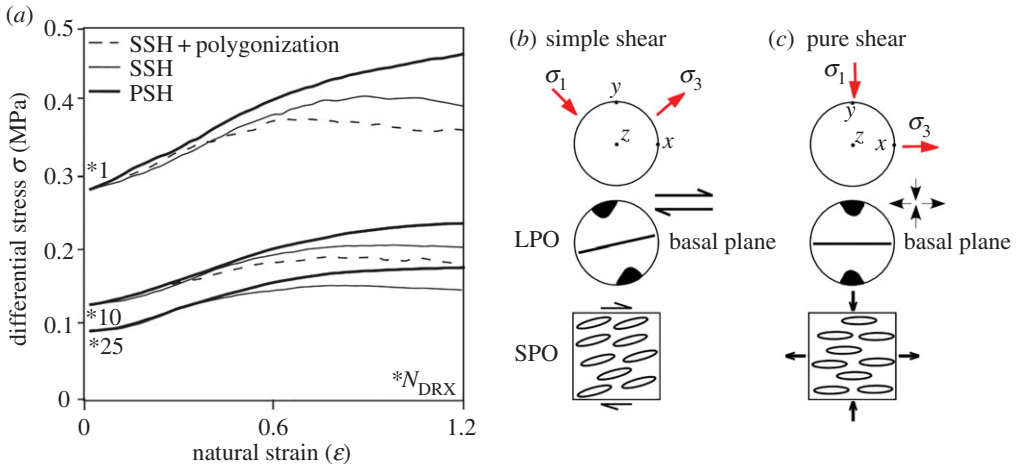


**Figure 8.** (a) Differential stress versus natural strain for all simulations. The ratio between DRX and FFT ( $N_{DRX}$ ) is indicated as 1, 10 or 25. A summary of the LPO and SPO developed with respect to the principal stresses is indicated in (b) for simple shear and (c) for pure shear numerical simulations. Differential stresses were normalized using the experimental values of [2]. (Online version in colour.)

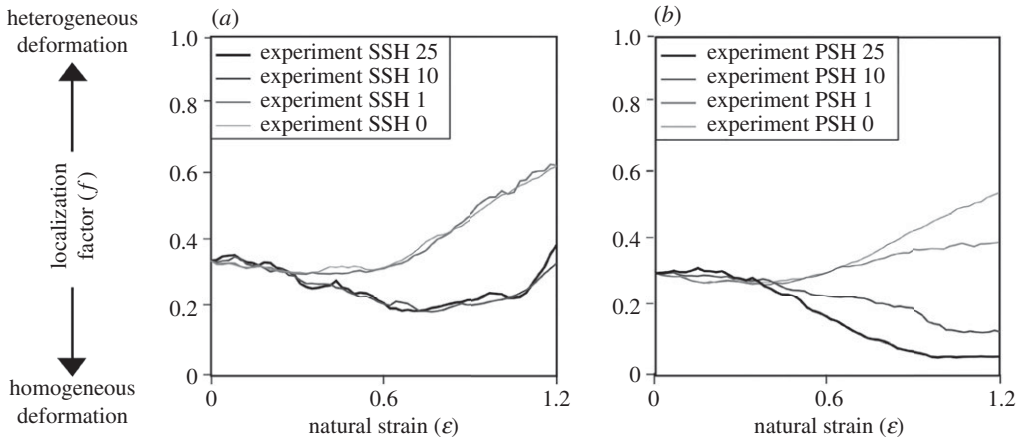


**Figure 9.** Localization factor ( $f$ ) evolution (equation (3.1)) during deformation for simulations with  $N_{DRX} = 0, 1, 10$  and 25 with (a) simple and (b) pure shear boundary conditions.

## (f) Ice simulations including polygonization

The influence of polygonization on the final microstructures was tested by analysing a series of simulations that include the ELLE polygonization subloop (i.e. experiments with suffix  $_N$ ). These models were carried out in both pure and simple shear deformation and with different amount of recrystallization: 1, 10 and 20 DRX steps per deformation step, respectively (figure 11*b,d,f*). When polygonization is active the differential stress reaches a steady state earlier than in the case of the corresponding simulation without this routine (dashed lines in figure 8). Polygonization does not affect the final strong LPO regardless the amount of DRX. This applies to both simple and pure shear cases (figure 11*a-d* and *e,f*, respectively). The lack of influence of polygonization is probably due to the fact that new grains have lattice orientations close to those of their parent grains. However, the incorporation of the polygonization process, and therefore the development

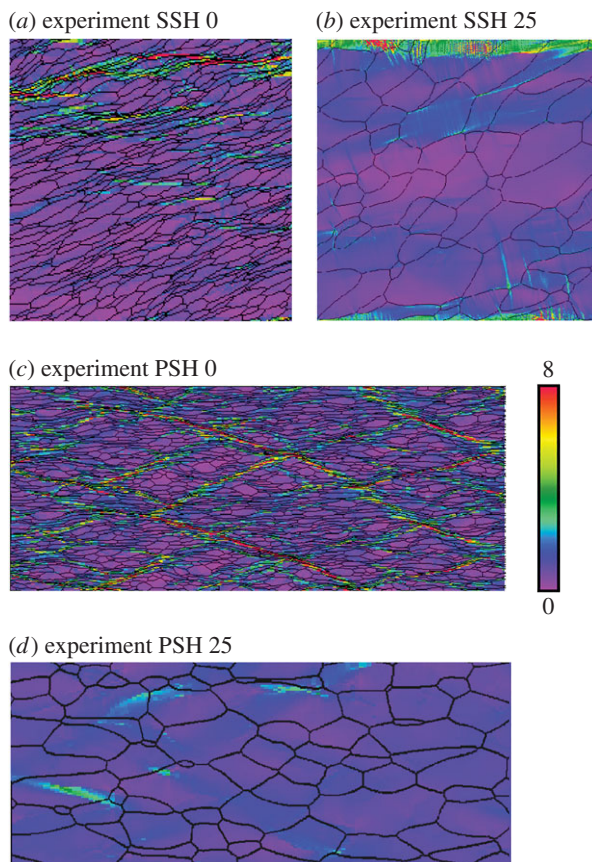


**Figure 10.** Maps of the von Mises strain-rate field normalized to the bulk von Mises strain rate at the final step (natural strain  $\varepsilon = 1.2$ ) are shown for (a,b) simple shear and (c,d) pure shear simulations with  $N_{\text{DRX}} = 0$  and 25. Colour coding is for local strain rate normalized to bulk strain rate. In pure shear simulations (c,d) the original image length is double that of the images shown. (Online version in colour.)

of proper HAGB out of tilt walls, reduces grain size compared to the cases in which this process is not included (table 2) [8]. Polygonization also changes the distribution of grain sizes, reducing the skewness and, in the case of the simple shear simulation SSH 10\_N, develops a bimodal distribution (figure 12b,c).

## 4. Discussion

### (a) Effects of ice flow on the lattice preferred orientation and final microstructure

Natural deformation in glaciers and ice sheets mostly occurs under general strain conditions between the end members pure and simple shear. In general, there is an increase in vorticity with depth, with pure shear dominating at the top and simple shear at the base (e.g. [53]). It is therefore important to understand how ice behaves differently under these varying boundary conditions, especially considering the strong anisotropy (LPO) developed in ice sheets and glaciers [3,54]. Our numerical results show that the boundary conditions do not significantly change the evolution of the microstructure due to viscoplastic deformation, because elongated grains and an SPO parallel to the stretching direction and normal to the finite shortening direction develop in both pure and simple shear cases. Qualitatively, increasing DRX in simple shear simulations results in an SPO oriented at a high angle with respect to the shear plane. Simple shear deformation results in a

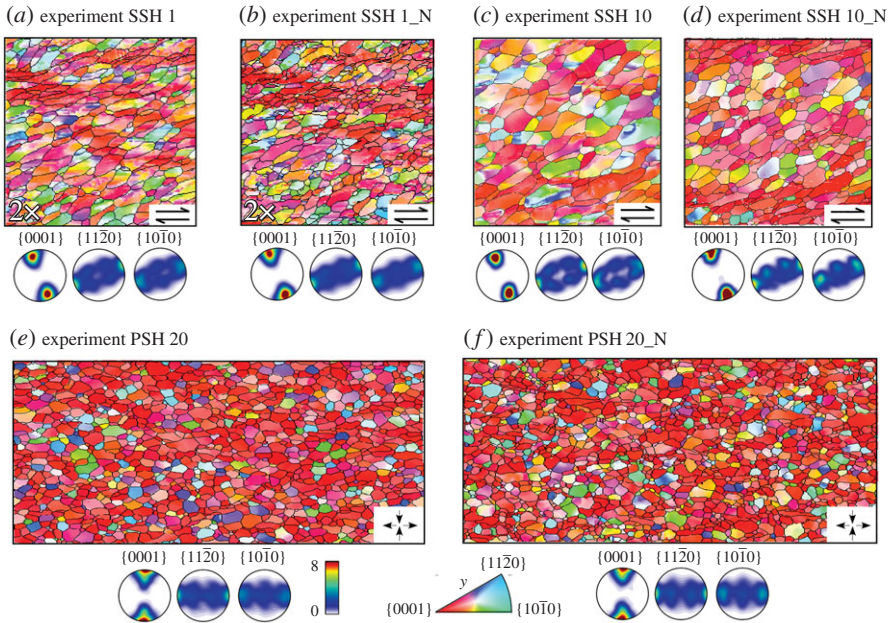


**Figure 11.** Lattice orientations relative to the  $y$ -direction (inverse poles) and pole figures of lattice orientation comparing the influence of incorporation of the polygonization process (indicated with suffix  $_N$ ). Simple shear simulations ( $a$ – $d$ ) reach a final natural strain of  $\varepsilon = 1.2$ , while pure shear simulations ( $e, f$ ) reach a final natural strain of  $\varepsilon = 0.75$ . The final LPO is not noticeably affected by polygonization, regardless of the amount of DRX: 1 ( $a, b$ ), 10 ( $c, d$ ) and 20 ( $e, f$ ). In order to allow visualization of the microstructures, the figures of experiments SSH 1 and SSH 1\_N, have been enlarged two times, only showing the upper left quarter of each model. Pole figures show orientation of unodes. (Online version in colour.)

rotation of the SPO towards the shear plane, according to the sense of shear (figures 3 and 4). GBM in isolation leads to an increase in grain size, as long as the grain boundary energy is a significant component of the driving force (equation (2.2)). It also reduces the grain elongation, hence masking strain localization. Although GBM is assumed to dominate in materials close to their melting point [55], recovery and polygonization probably play a significant role in ice sheets and glaciers. They counteract the GBM-induced grain growth, leading to a steady grain size where a balance is reached [32,56]. Adding polygonization to the model indeed leads to a reduction in grain size and grain elongation, although a steady state is not (yet) reached in our simulations (figures 11 and 12). The results are consistent with the observation that GBM and polygonization are active in large parts of ice sheets, as indicated by the absence of elongated grains in most ice core microstructures observed to date (e.g. [5,57]). Moreover, polygonization has recently been found to be also active in experimental ice creep tests close to the melting point [58].

In our simulations, a strong  $c$ -axes maximum initially develops parallel to the maximum compressive direction ( $\sigma_1$ ) at a natural strain of  $\varepsilon = 0.3$  in pure shear boundary conditions. When DRX is active this single maximum tends to shift towards being obliquely oriented with respect to  $\sigma_1$  (or  $X$  axis) in the  $YZ$  plane (figure 5). Pure shear and uniaxial compression experiments [59,60] of polycrystalline ice result in a girdle fabric of  $c$ -axes around the direction of  $\sigma_1$  (compression direction). The lack of  $c$ -axes oriented parallel to  $\sigma_1$  in our simulations is interpreted as due to the activation of recrystallization processes, coherently with temperatures near to the melting point in the experiments (between  $-2^\circ\text{C}$  and  $-7^\circ\text{C}$ ).

In simple shear, the  $c$ -axes maximum initially develops parallel to  $\sigma_1$ , but rapidly tends to rotate with increasing strain towards being oblique or normal to the shear plane (figure 5). Similarly to the pure shear cases, activation of recrystallization processes shifts the maximum towards being oblique to the  $XY$  section. Ice deformation laboratory experiments revealed a

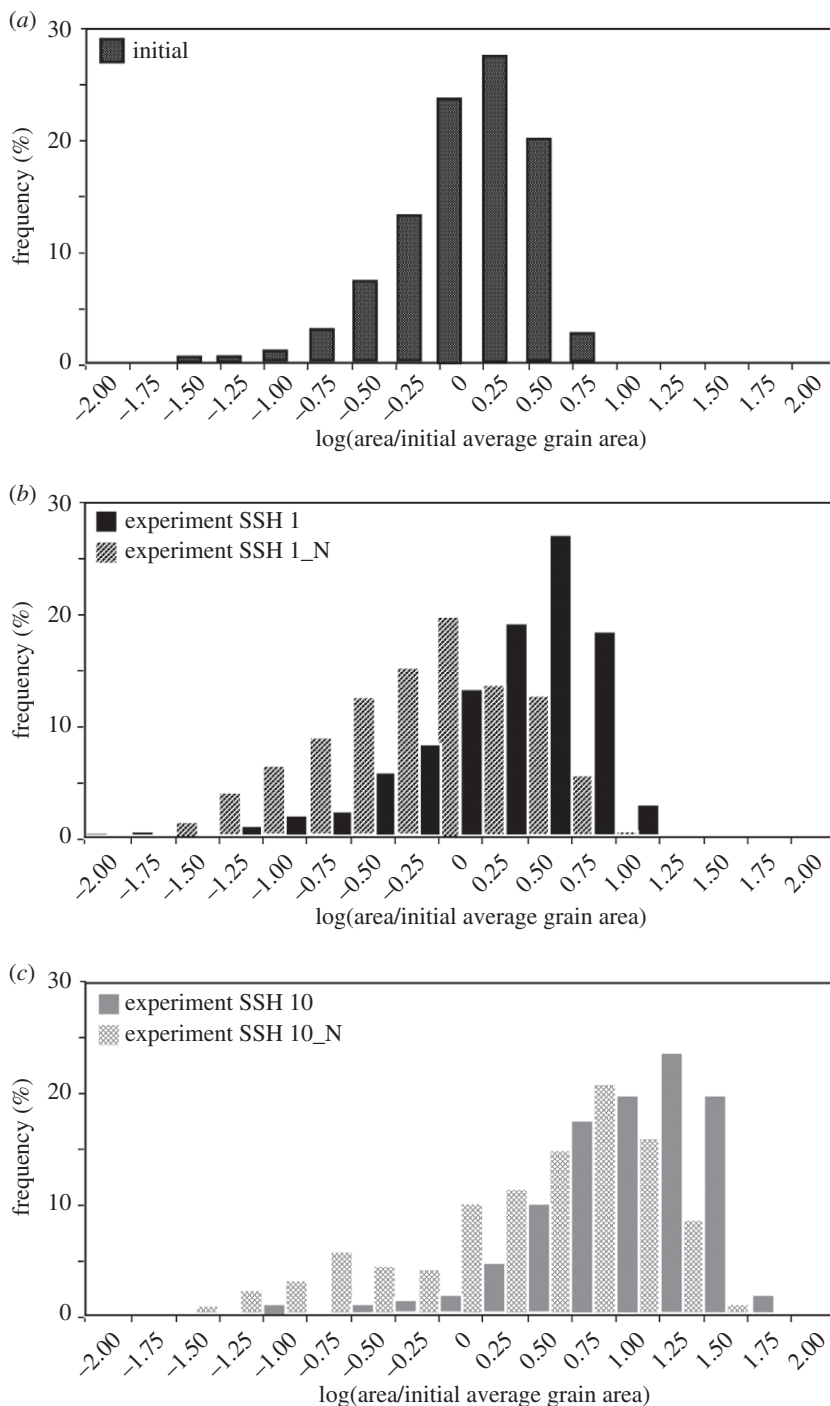


**Figure 12.** Comparison of the final grain area distribution normalized to the initial average grain area at the start of the simulation (a) and at the end of the simulations, performed without or with polygonization (indicated with suffix \_N), for (b) 1 step or (c) 10 steps of DRX per deformation. Initial distribution in (a).

similar pattern in simple shear, with the  $c$ -axes maximum oriented normal to the shear plane but also obliquely oriented with respect to  $\sigma_1$  (e.g. [61,62]).

Once an LPO forms, it does strengthen and rotate with increasing deformation according to the sense of shear in simple shear simulations (figures 4 and 5). The rotational evolution of ice

fabrics in simple shear is typically characterized by the development of a strong single maximum approximately perpendicular to the shear direction [61]. With increasing strain, the obliquely oriented maximum disappears in experiments and only the maximum oriented perpendicular to the shear plane remains [61]. This observation differs from our simulations, in which the  $c$ -axes maximum is always obliquely oriented. This rotational evolution of ice fabrics has been recognized as vertical or near vertical single maximum LPOs in ice cores [5,63–66]. The vorticity of deformation is typically close to simple shear in the deep part of ice sheets, with the shear plane generally oriented parallel to the bedrock [57]. Another difference between laboratory experiments and numerical simulations is that the first only consider uniaxial deformation while simulations are performed under perfect two-dimensional plane strain (i.e. pure shear).

The statement that a single maximum LPO like that observed in nature under simple shear cannot be simulated unless recrystallization is taken into account [4] is not consistent with the results of our simulations, as the developing hard grains further rotate according to the sense of shear independently of the intensity of recrystallization  $N_{\text{DRX}}$  (figure 5, at a natural strain of  $\varepsilon = 1.2$ ).

Our simulations show how such LPOs develop as a consequence of deformation, even when there is strong recrystallization. The implementation of the polygonization routine does not affect the developed LPO, because new grains that nucleate maintain the  $c$ -axis orientations close to that of their parental grains (figure 11*b,d,f*). An additional factor controlling the development of an LPO is the degree of strain localization, as illustrated by the difference in LPO developed in high and low strain-rate domains (e.g. figure 5*i,j*). The detailed evolution of the LPOs in different scenarios of strain localization needs to be systematically addressed in future studies.

## (b) Effects of vorticity of ice flow on rheology

All simulations present strain hardening behaviour during the first stages of deformation (figure 8), during which the degree of deformation localization remains relatively constant (figure 9*a,b*). At a natural strain of  $\varepsilon = 0.3$  an LPO can be identified in both pure and simple shear simulations (figure 5), which result in the development of an intrinsic anisotropy that leads to an increment of strain localization in simulations performed at high strain rates (i.e. experiments SSH and PSH 0 and 1; figure 9). Differential stress reaches a steady state in simple shear simulations (figure 8*a*). This is associated with the rotation of the LPO and SPO to a more favourable position for slip, as basal planes and elongated grains progressively rotate towards the shear direction (figure 4*a–d*). However, the SPO and LPO develop in a less favourable orientation for easy glide in pure shear models, where they tend to rotate away from  $\sigma_1$  (figure 4*e–h*). In such cases, strain hardening keeps increasing until the end of the simulations (figure 8*a*). The development of an SPO perpendicular to the compression direction has been proposed as the cause of strain hardening in previous studies [50,67]. The formation of new grain boundaries by polygonization has a clear influence on the rheology, where the differential stress reaches a steady state earlier than in the equivalent simulation without polygonization (dashed lines figure 8*a*). This steady state is achieved when an equilibrium in grain size is reached [68], which depends on the relative amount of new grains nucleated by polygonization versus GBM [5].

A hardening-and-softening behaviour is observed in laboratory experiments under constant stress or constant strain rate in both pure and simple shear configurations [60]. In experiments, a stress peak is typically observed below a strain of 0.04. In our simulations, the transition between hardening and softening is observed at a higher strain, at approximately 0.30. There are some remarkable differences between laboratory experiments and numerical simulations. One of them is that in our models, we assume lower strain-rate conditions ( $10^{-10}$  to  $10^{-12}$  s $^{-1}$ ) than those used in laboratory experiments, where higher strain rates are used ( $10^{-5}$  and  $10^{-7}$  s $^{-1}$ ). This implies that our assumption of viscoplastic behaviour of ice polycrystals is perhaps not valid for the range of strain rates used in laboratory experiments, although it is more realistic for comparisons with natural cases. In these conditions, transient creep must be considered and an elastoviscous–plastic behaviour is more appropriate to describe the mechanical behaviour

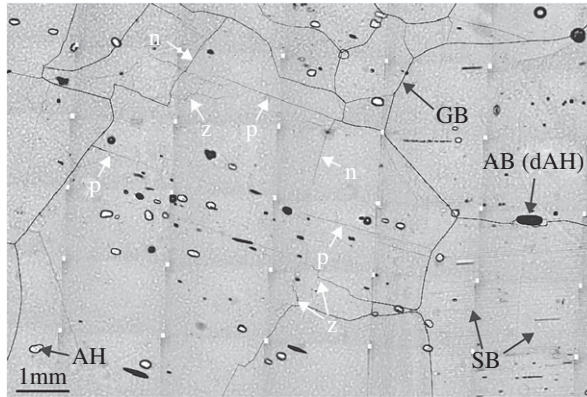


**Figure 13.** Example of subgrain boundary types in EDML ice core. n, Normal to basal plane ‘Nakaya’ type; p, parallel to basal plane type; z, mixed type. Further details see [74,75].

of the ice polycrystalline aggregate. For example, in [69], an elastoviscous–plastic model was used to simulate transient creep from the experimental data of [70]. However, this approach is limited to very low strains (less than 0.05), significantly lower than those expected in natural ice sheets. Another key difference is that a hardening-and-softening behaviour is always observed in laboratory experiments regardless the stress configuration. Contrarily, this is only observed in our models in simple shear conditions. We have to take into account that the strain rate and geometry of deformation are constant during the simulation time. Only strain hardening occurs in numerical pure shear models, at least up to the end of the simulation time ( $\varepsilon = 1.2$ ). Our results indicate that tertiary creep is probably not steady state, and that hardening and softening can probably occur at large strain. This would be associated with an increase of the strength of the LPO and the viscous anisotropy of the material.

Simulations performed at low strain rates do not show high-strain localization bands (figure 10*b–d*), as deformation is more homogeneously distributed (figure 9, experiments SSH and PSH 10 and 25). GBM and polygonization result in microstructures dominated by larger and more equidimensional grains, preventing the formation of strong grain elongation and masking localization bands. In that situation and with a strong LPO, deformation cannot be accommodated by high-strain bands any more, leading to the activation of the non-basal slip systems in both pure and simple shear simulations (figure 6*b*). The favourable orientation of the pyramidal plane with respect to  $\sigma_1$  in pure shear models (figure 5*e–h*) enables dislocations to glide along this system of planes rather than along the basal ones (figure 6*b*, dashed lines). However, the pyramidal plane does not reach this favourable orientation with respect to  $\sigma_1$  in simple shear simulations, due to the rotation of the LPO with the sense of shear (figure 5*a–d*). This results in the basal slip system remaining more active than the non-basal ones throughout the simulations (figure 6*b*, solid lines). This evolution of changing slip system activity has to be further investigated, as its occurrence has been proposed to be a rate-limiting mechanism not only at high stresses [71], but also applicable to low stress conditions.

The activation of non-basal slip systems can be recognized from the rotation of the *a*-axes towards the maximum elongation axis, while *c*-axes rotate towards the direction of the maximum finite shortening (figure 4*c,d,g,h*). Recently, clustering of *a*-axes in a wide girdle at a high angle to the compression direction was observed in experiments with DRX analysed by electron backscatter diffraction (EBSD) [58]. Clustering of *a*-axes has been previously described in the deep part of the GRIP ice core, where the slip along non-basal systems is proposed as a possible cause of the *a*-axis concentration [72]. The activation of the non-basal slip systems is related to the development of subgrain boundaries, as shown in figure 7*b,d*. Subgrain boundaries composed of basal (tilt and twist boundaries) and non-basal dislocations (tilt boundaries) were described

using EBSD datasets, where the non-basal dislocations play an important role in the formation of all subgrain boundaries [73,74]. The frequent abundance of different subgrain boundary types (figure 13), especially the ‘p-type’ subgrain boundaries (more than 50% of all subgrain boundaries in EDML [75]), which cannot be basal twist boundaries only but also non-basal tilt boundaries (more than 75% according to very first estimates, table 2 [74]), gives indications of the importance of non-basal dislocation activity. This has to be treated with care, as only recovered dislocations can be measured, forming subgrain boundaries, and not all dislocations involved in deformation. Clearly, more high-resolution full-crystal orientation measurements are needed to validate our models with respect to magnitude of recovery versus the activation of different slip systems during deformation.

## 5. Conclusion

We present a state of the art of a full-field numerical approach applied to ice. It includes simulations with and without recrystallization under pure and simple shear boundary conditions. Although the amount of recrystallization strongly affects the grain morphology, it has a much smaller effect on LPO development. In all cases, regardless of the amount of DRX and ice flow, a single *c*-axes maximum develops that is oriented approximately perpendicular to the maximum finite shortening direction and which in simple shear rotates towards the normal to the shear plane. This leads to distinctly different behaviour in pure and simple shear. In pure shear, the LPO and SPO are increasingly unfavourable for deformation, leading to hardening and to an increased activity of non-basal slip. The opposite happens in simple shear, where vorticity causes rotation of the LPO and SPO to a favourable orientation resulting in strain softening. The increase of recrystallization enhances the activity of the non-basal slip, due to the reduction of deformation localization. In pure shear conditions the pyramidal slip activity is thus even more enhanced and can become higher than the basal-slip activity.

Our results further show that subgrain boundaries can be developed by the activity of the non-basal slip systems. The implementation of the polygonization routine reduces grain size and SPO, but does not significantly change the final LPO, because newly nucleated grains approximately keep the *c*-axis orientations of their parental grains. However, it enables the establishment of a grain size equilibrium, and therefore the differential stress reaches a steady state.

**Authors' contributions.** M.-G.L., P.D.B., A.G. and I.W. conceived the study. M.-G.L. wrote the manuscript together with A.G., P.D.B., E.G.R. and I.W. D.J. and R.A.L. critically discussed the content and edited the manuscript. A.G., R.A.L., M.-G.L., P.D.B., J.R., E.G.R. and F.S. contributed to the development of the numerical codes. All authors gave final approval for publication.

**Competing interests.** The authors declare that there are no competing interests.

**Funding.** M.-G.L. was funded by the programme on Recruitment of Excellent Researchers of the Eberhard Karls Universität Tübingen. F.S. was funded by DFG (SPP 1158) grant BO 1776/12-1. The Microdynamics of Ice (MicroDICE) research network, funded by the European Science Foundation, is acknowledged for funding research visits of M.-G.L.

**Acknowledgements.** We thank all the members of the ELLE development group, in particular, Lynn Evans, Sandra Piazzolo and Verity Borthwick for their contributions to the simulation code. We gratefully acknowledge A. Treverrow and an anonymous reviewer, whose constructive reviews greatly improved the manuscript, together with the editorial guidance of P. Sammonds. This work was carried out as part of the Helmholtz Junior Research group ‘The effect of deformation mechanisms for ice sheet dynamics’ (VH-NG-802).

## References

1. Schulson EM, Duval P. 2009 *Creep and fracture of ice*, vol. 432. Cambridge, UK: Cambridge University Press.
2. Duval P, Ashby M, Anderman I. 1983 Rate controlling processes in the creep of polycrystalline ice. *J. Phys. Chem.* **87**, 4066–4074. (doi:10.1021/ j100244a014)
3. Faria SH, Kipfstuhl S, Azuma N, Freitag J, Hamann I, Murshed MM, Kuhs WF. 2009 The multiscale structure of Antarctica. Part I: inland ice. *Low Temp. Sci.* **68**, 39–59.

4. Van der Veen CJ, Whillans IM. 1994 Development of fabric in ice. *Cold Reg. Sci. Technol.* **22**, 171–195. (doi:10.1016/0165-232X(94)90027-2)
5. Faria SH, Weikusat I, Azuma N. 2014 The microstructure of polar ice. Part II: state of the art. *J. Struct. Geol.* **61**, 21–49. (doi:10.1016/j.jsg.2013.11.003)
6. Duval P, Castelnau O. 1995 Dynamic recrystallization of ice in polar ice sheets. *J. Phys. IV* **5**, C3-197–C3-205. (doi:10.1051/jp4:1995317)
7. Duval P, Arnaud L, Brissaud O, Montagnat M, de La Chapelle S. 2000 Deformation and recrystallization processes of ice from polar ice sheets. *Ann. Glaciol.* **30**, 83–87. (doi:10.3189/172756400781820688)
8. Llorens M-G, Grier A, Bons PD, Roessiger J, Lebensohn R, Evans L, Weikusat I. 2016 Dynamic recrystallisation of ice aggregates during co-axial viscoplastic deformation: a numerical approach. *J. Glaciol.* **62**, 359–377. (doi:10.1017/jog.2016.28)
9. Faria SH, Freitag J, Kipfstuhl S. 2010 Polar ice structure and the integrity of ice-core paleoclimate records. *Quat. Sci. Rev.* **29**, 338–351. (doi:10.1016/j.quascirev.2009.10.016)
10. Waddington ED, Bolzan JF, Alley RB. 2001 Potential for stratigraphic folding near ice-sheet centers. *J. Glaciol.* **47**, 639–648. (doi:10.3189/172756501781831756)
11. Alley RB, Gow AJ, Meese DA, Fitzpatrick JJ, Waddington ED, Bolzan JF. 1997 Grain-scale processes, folding, and stratigraphic disturbance in the GISP2 ice core. *J. Geophys. Res.* **102**, 26 819–26 830. (doi:10.1029/96JC03836)
12. Bons PD *et al.* 2016 Converging flow and anisotropy cause large-scale folding in Greenland's ice sheet. *Nat. Commun.* **7**, 11427. (doi:10.1038/NCOMMS11427)
13. Budd W, Jacka T. 1989 A review of ice rheology for ice sheet modelling. *Cold Reg. Sci. Technol.* **16**, 107–144. (doi:10.1016/0165-232X(89)90014-1)
14. Etheridge DM. 1989 Dynamics of the Law Dome ice cap, Antarctica, as found from bore-hole measurements. *J. Glaciol.* **12**, 46–50.
15. Jacka TH. 1984 Laboratory studies on relationships between ice crystal size and flow rate. *Cold Reg. Sci. Technol.* **10**, 31–42. (doi:10.1016/0165-232X(84)90031-4)
16. Azuma N. 1994 A flow law for anisotropic ice and its application to ice sheets. *Earth Planet. Sci. Lett.* **128**, 601–614. (doi:10.1016/0012-821X(94)90173-2)
17. Treverrow A, Budd WF, Jacka TH, Warner RC. 2012 The tertiary creep of polycrystalline ice: experimental evidence for stress-dependent levels of strain-rate enhancement. *J. Glaciol.* **58**, 301–314. (doi:10.3189/2012JoG11J149)
18. Montagnat M, Duval P. 2004 The viscoplastic behaviour of ice in polar ice sheets: experimental results and modelling. *C. R. Phys.* **5**, 699–708. (doi:10.1016/j.crhy.2004.06.002)
19. Glen JW. 1955 The creep of polycrystalline ice. *Proc. R. Soc. Lond. A* **228**, 519–538. (doi:10.1098/rspa.1955.0066)
20. Montagnat M *et al.* 2013 Multiscale modeling of ice deformation behavior. *J. Struct. Geol.* **61**, 78–108. (doi:10.1016/j.jsg.2013.05.002)
21. Castelnau O, Duval P, Montagnat M, Brenner R. 2008 Elastoviscoplastic micromechanical modeling of the transient creep of ice. *J. Geophys. Res.* **113**, B11203. (doi:10.1029/2008JB005751)
22. Becker R. 1991 Analysis of texture evolution in channel die compression. 1. Effects of grain interaction. *Acta Metall. Mater.* **39**, 1211–1230. (doi:10.1016/0956-7151(91)90209-J)
23. Diard O, Leclercq S, Rousselier G, Cailletaud G. 2005 Evaluation of finite element based analysis of 3D multicrystalline aggregates plasticity. Application to crystal plasticity model identification and the study of stress and strain fields near grain boundaries. *Int. J. Plast.* **21**, 691–722. (doi:10.1016/j.ijplas.2004.05.017)
24. Moulinec H, Suquet P. 1994 A fast numerical method for computing the linear and nonlinear mechanical properties of composites. *C. R. Acad. Sci. II* **318**, 1417–1423.
25. Lebensohn RA. 2001 N-site modelling of a 3D viscoplastic polycrystal using fast Fourier transform. *Acta Mater.* **49**, 2723–2737. (doi:10.1016/S1359-6454(01)00172-0)
26. Lebensohn RA, Liu Y, Castañeda PP. 2004 Macroscopic properties and field fluctuations in model power-law polycrystals: full-field solutions versus self-consistent estimates. *Proc. R. Soc. Lond. A* **460**, 1381–1405. (doi:10.1098/rspa.2003.1212)
27. Jansen D, Llorens M-G, Westhoff J, Steinbach F, Kipfstuhl S, Bons PD, Grier A, Weikusat, I. 2015 Small-scale disturbances in the stratigraphy of the NEEM ice core: observations

- and numerical model simulations. *Cryosphere* **10**, 359–370. (doi:10.5194/tc-10-359-2016)
28. Jessell MW, Bons PD, Evans L, Barr T, Stüwe K. 2001 Elle: the numerical simulation of metamorphic and deformation microstructures. *Comput. Geosci.* **27**, 17–30. (doi:10.1016/S0098-3004(00)00061-3)
  29. Bons PD, Koehn D, Jessell MW (eds). 2008 *Microdynamic simulation*. Lecture Notes in Earth Sciences, vol. 106. Berlin, Germany: Springer. (doi:10.1007/978-3-540-44793-1)
  30. Bons PD, Jessell MW, Evans L, Barr TD, Stüwe K. 2001 Modelling of anisotropic grain growth in minerals. *Geol. Soc. Am. Mem.* **193**, 39–49.
  31. Jessell MW, Kostenko O, Jamtveit B. 2003 The preservation potential of microstructures during static grain growth. *J. Metamorph. Geol.* **21**, 481–491. (doi:10.1046/j.1525-1314.2003.00455.x)
  32. Roessiger J, Bons PD, Griera A, Jessell MW, Evans L, Montagnat M, Kipfstuhl S, Faria SH, Weikusat I. 2011 Competition between grain growth and grain size reduction in polar ice. *J. Glaciol.* **57**, 942–948. (doi:10.3189/002214311798043690)
  33. Becker JK, Bons PD, Jessell MW. 2008 A new front-tracking method to model anisotropic grain and phase boundary motion in rocks. *Comput. Geosci.* **34**, 201–212. (doi:10.1016/j.cageo.2007.03.013)
  34. Piazzolo S, Bons PD, Jessell MW, Evans L, Passchier CW. 2002 Dominance of microstructural processes and their effect on microstructural development: insights from numerical modelling of dynamic recrystallization. *Geol. Soc. Lond. Spec. Publ.* **200**, 149–170. (doi:10.1144/GSL.SP.2001.200.01.10)
  35. Llorens M-G, Bons PD, Griera A, Gomez-Rivas E, Evans LA. 2013 Single layer folding in simple shear. *J. Struct. Geol.* **50**, 209–220. (doi:10.1016/j.jsg.2012.04.002)
  36. Llorens M-G, Bons PD, Griera A, Gomez-Rivas E. 2013 When do folds unfold during progressive shear? *Geology* **41**, 563–566. (doi:10.1130/G33973.1)
  37. Griera A, Bons PD, Jessell MW, Lebensohn RA, Evans L, Gomez-Rivas E. 2011 Strain localization and porphyroblast rotation. *Geology* **39**, 275–278. (doi:10.1130/G31549.1)
  38. Griera A, Llorens M-G, Gomez-Rivas E, Bons PD, Jessell MW, Evans LA, Lebensohn RA. 2013 Numerical modelling of porphyroblast and porphyroblast rotation in anisotropic rocks. *Tectonophysics* **587**, 4–29. (doi:10.1016/j.tecto.2012.10.008)
  39. Lebensohn RA, Brenner R, Castelnau O, Rollett AD. 2008 Orientation image-based micromechanical modelling of subgrain texture evolution in polycrystalline copper. *Acta Mater.* **56**, 3914–3926. (doi:10.1016/j.actamat.2008.04.016)
  40. Mainprice D, Hielscher R, Schaeben H. 2011 Calculating anisotropic physical properties from texture data using the MTEX open source package. *Geol. Soc. Lond. Spec. Publ.* **360**, 175–192. (doi:10.1144/SP360.10)
  41. Glen JW. 1952 Experiments on the deformation of ice. *J. Glaciol.* **2**, 111–114.
  42. Urai JL, Means WD, Lister GS. 1986 Dynamic recrystallization of minerals. In *Mineral and rock deformation: laboratory studies* (eds BE Hobbs, HC Heard). Geophysical Monograph, no. 36, pp. 161–199. Washington, DC: American Geophysical Union.
  43. Borthwick VE, Piazzolo S, Evans L, Griera A, Bons PD. 2013 What happens to deformed rocks after deformation? A refined model for recovery based on numerical simulations. *Geol. Soc. Lond. Spec. Publ.* **394**, 215–534. (doi:10.1144/SP394.11)
  44. Nasello OB, Di Prinzio CL, Guzmán PG. 2005 Temperature dependence of ‘pure’ ice grain boundary mobility. *Acta Mater.* **53**, 4863–4869. (doi:10.1016/j.actamat.2005.06.022)
  45. Thorsteinsson T. 2002 Fabric development with nearest-neighbor interaction and dynamic recrystallization. *J. Geophys. Res.* **107**, ECV 3-1–ECV 3-13. (doi:10.1029/2001JB000244)
  46. Randle V. 1993 Microtexture investigation of the relationship between strain and anomalous grain growth. *Philos. Mag. A* **67**, 1301–1313. (doi:10.1080/01418619308225356)
  47. Hansen LN, Warren JM, Zimmerman ME, Kohlstedt DL. 2016 Viscous anisotropy of textured olivine aggregates. Part 1: measurement of the magnitude and evolution of anisotropy. *Earth Planet. Sci. Lett.* **445**, 92–103. (doi:10.1016/j.epsl.2016.04.008)
  48. Skemer P, Sundberg M, Hirth G, Cooper R. 2011 Torsion experiments on coarse-grained dunite: implications for microstructural evolution when diffusion creep is suppressed. *Geol. Soc. Lond. Spec. Publ.* **360**, 211–223. (doi:10.1144/SP360.12)
  49. Holyoke CW, Tullis J. 2006 Mechanisms of weak phase interconnection and the effects of phase strength contrast on fabric development. *J. Struct. Geol.* **28**, 621–640. (doi:10.1016/j.jsg.2006.01.008)

50. Takeda YT, Griera A. 2006 Rheological and kinematical responses to flow of two-phase rocks. *Tectonophysics* **427**, 95–113. (doi:10.1016/j.tecto.2006.03.050)
51. Sornette A, Davy P, Sornette D. 1993 Fault growth in brittle-ductile experiments and the mechanics of continental collisions. *J. Geophys. Res. Solid Earth* **98**, 12111–12139. (doi:10.1029/92JB01740)
52. Gomez-Rivas E. 2008 Localización de la deformación en medios dúctiles y anisótropos: estudio de campo, experimental y numérico. Trabajo doctoral, Universitat Autònoma de Barcelona, Spain.
53. Cuffey K, Paterson WSB. 2010 *The physics of glaciers*. New York, NY: Academic Press.
54. NEEM Community Members. 2013 Eemian interglacial reconstructed from a Greenland folded ice core. *Nature* **493**, 489–494. (doi:10.1038/nature11789)
55. Humphreys FJ, Hatherly M. 2004 *Recrystallization and related annealing phenomena*, 2nd edn. Oxford, UK: Pergamon Press.
56. Mathiesen J, Ferkinghoff-Borg J, Jensen MH, Levinsen M, Olesen P, Dahl-Jensen D, Svensson A. 2004 Dynamics of crystal formation in the Greenland NorthGRIP ice core. *J. Glaciol.* **50**, 325–328. (doi:10.3189/172756504781829873)
57. Weikusat I *et al.* 2017 Physical analysis of an Antarctic ice core—towards an integration of micro- and macrodynamics of polar ice. *Phil. Trans. R. Soc. A* **375**, 20150347. (doi:10.1098/rsta.2015.0347)
58. Montagnat M, Chauve T, Barou F, Tommasi A, Beausir B, Fressengeas C. 2015 Analysis of dynamic recrystallization of ice from EBSD orientation mapping. *Front. Earth Sci.* **3**, 81. (doi:10.3389/feart.2015.00081)
59. Jacka TH, Maccagnan M. 1984 Ice crystallographic and strain rate changes with strain in compression and extension. *Cold Reg. Sci. Technol.* **8**, 269–286. (doi:10.1016/0165-232X(84)90058-2)
60. Piazzolo S, Wilson CJ, Luzin V, Brouzet C, Peternell M. 2013 Dynamics of ice mass deformation: linking processes to rheology, texture, and microstructure. *Geochem. Geophys. Geosyst.* **14**, 4185–4194. (doi:10.1002/ggge.20246)
61. Bouchez JL, Duval P. 1982 The fabric of polycrystalline ice deformed in simple shear: experiments in torsion, natural deformation and geometrical interpretation. *Texture Stress Microstruct.* **5**, 171–190. (doi:10.1155/TSM.5.171)
62. Wilson CJ, Peternell M. 2012 Ice deformed in compression and simple shear: control of temperature and initial fabric. *J. Glaciol.* **58**, 11–22. (doi:10.3189/2012JoG11J065)
63. Fitzpatrick JJ *et al.* 2014 Physical properties of the WAIS Divide ice core. *J. Glaciol.* **60**, 1181–1198. (doi:10.3189/2014JoG14J100)
64. Herron SL, Langway CC. 1982 A comparison of ice fabrics and textures at Camp Century, Greenland and Byrd Station, Antarctica. *Ann. Glaciol.* **3**, 118–124. (doi:10.3198/1982AoG3-1-118-124)
65. Montagnat M *et al.* 2014 Fabric along the NEEM ice core, Greenland, and its comparison with GRIP and NGRIP ice cores. *Cryosphere* **8**, 1129–1138. (doi:10.5194/tc-8-1129-2014)
66. Thorsteinsson T, Kipfstuhl J, Miller H. 1997 Textures and fabrics in the GRIP ice core. *J. Geophys. Res.* **102**, 26 583–26 599. (doi:10.1029/97JC00161)
67. Treagus SH, Lan L. 2004 Deformation of square objects and boudins. *J. Struct. Geol.* **26**, 1361–1376. (doi:10.1016/j.jsg.2003.12.002)
68. Jacka TH, Li J. 1994 The steady-state crystal size of deforming ice. *Ann. Glaciol.* **20**, 13–28. (doi:10.3189/172756494794587230)
69. Suquet P, Moulinec H, Castelnau O, Montagnat M, Lahellec N, Grennerat F, Duval P, Brenner R. 2012 Multi-scale modeling of the mechanical behavior of polycrystalline ice under transient creep. *Proc. IUTAM* **3**, 76–90. (doi:10.1016/j.piutam.2012.03.006).
70. Weertman J. 1973 Creep of ice. In *Physics and chemistry of ice* (eds E Whalley, S Jones, L Gold), pp. 320–337. Ottawa, Canada: Royal Society of Canada.
71. Montagnat M, Duval P. 2000 Rate controlling processes in the creep of polar ice, influence of grain boundary migration associated with recrystallization. *Earth Planet. Sci. Lett.* **183**, 179–186. (doi:10.1016/S0012-821X(00)00262-4)
72. Miyamoto A, Shoji H, Hori A, Hondoh T, Clausen HB, Watanabe O. 2005 Ice fabric evolution process understood from anisotropic distribution of a-axis orientation on the GRIP (Greenland) ice core. *Ann. Glaciol.* **42**, 47–52. (doi:10.3189/172756405781812501)

73. Weikusat I, De Winter DAM, Pennock GM, Hayles M, Schneijdenberg CTWM, Drury MR. 2011 Cryogenic EBSD on ice: preserving a stable surface in a low pressure SEM. *J. Microsc.* **242**, 295–310. (doi:10.1111/j.1365-2818.2010.03471.x)
74. Weikusat I, Miyamoto A, Faria SH, Kipfstuhl S, Azuma N, Hondoh T. 2011 Subgrain boundaries in Antarctic ice quantified by X-ray Laue diffraction. *J. Glaciol.* **57**, 111–120. (doi:10.3189/002214311795306628)
75. Weikusat I, Kipfstuhl S, Faria SH, Azuma N, Miyamoto A. 2009 Subgrain boundaries and related microstructural features in EDML (Antarctica) deep ice core. *J. Glaciol.* **55**, 461–472. (doi:10.3189/002214309788816614)